CHEMISTRY OF MATERIALS

pubs.acs.org/cm

Article

# Oxygen Absorption in Nanocrystalline h-$RMnO_3$ ($R$ = Y, Ho, Dy) and the Effect of Ti Donor Doping

Frida Hemstad Danmo, Benjamin A. D. Williamson, Didrik R. Småbråten, Nikolai H. Gaukås, Elise R. Østli, Tor Grande, Julia Glaum, and Sverre M. Selbach*

Cite This: *Chem. Mater.* 2023, 35, 5764−5776

Read Online

ACCESS | Metrics & More | Article Recommendations | Supporting Information

**ABSTRACT:** Hexagonal manganites, $RMnO_3$ ($R$ = Sc, Y, Ho-Lu), can reversibly store and release large quantities of oxygen at temperatures in the range of 150−400 °C. The oxygen storage properties can be tuned by combining different $R^{3+}$ cations, aliovalent dopants, and crystallite sizes in the nanometer range. Here, we study the oxygen absorption of nanocrystalline $RMn_{1-x}Ti_xO_3$ ($R$ = Y, Ho, Dy; $x$ = 0, 0.15) using thermogravimetric analysis (TGA) and high-temperature X-ray diffraction (HT-XRD) in $O_2$ and $N_2$ atmospheres. The maximum oxygen storage capacity increases from $R$ = Y through Ho and Dy and even further with $Ti^{4+}$ as a donor dopant. Density functional theory (DFT) calculations show that the observed trends in oxygen absorption capacity are correlated with the enthalpy of oxidation and the lattice parameters. $Ti^{4+}$ also increases the thermal stability of absorbed oxygen and thereby extends the operation range to higher temperatures where the absorption and desorption kinetics are faster. Reducing the size of the crystallites improves the oxygen storage capacity as well as the absorption kinetics due to shorter diffusion distances. Finally, a thermodynamic model for the oxidation of $RMnO_3$ is presented and fitted to TGA data and the implications for the microscopic understanding of the oxidation process are discussed.

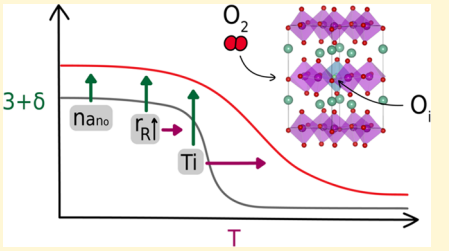


## INTRODUCTION

Oxides that can reversibly store and release oxygen at elevated temperatures find a broad range of applications, such as chemical looping combustion (CLC) for the production of hydrogen and syngas, the separation of oxygen from air using pressure swing adsorption (PSA), as automotive exhaust catalysts, and as electrodes in solid oxide fuel cells (SOFCs).[1−5] $CeO_2$ and $CeO_2$−$ZrO_2$ solid solutions are among the most studied oxygen carriers and have been widely used for the treatment of exhaust gas but are prone to a decrease in surface area due to particle coarsening at higher temperatures, causing an efficiency loss at lower temperatures and an increase in exhaust fumes.[6,7] For high-temperature applications like pressure swing adsorption, sorbents such as those based on the $La_{1-x}Sr_xCo_{1-y}FeyO_{3-\delta}$ (LSCF) perovskite system[5,8−10] and double perovskites such as $BaYMn_2O_{5+\delta}$[11] have been widely studied. Common to these material systems is that oxygen vacancies are the main point defects involved in oxygen storage and transport, and the concentration of vacancies can be tuned by aliovalent dopants.[6] The limited diffusivity of oxygen vacancies limits the lower-temperature range of operation for these materials, and cation mobility at the necessary operating temperatures can lead to degradation in the form of coarsening, kinetic demixing,[12] and surface segregation.[13]

Hexagonal manganites with composition $RMnO_3$ ($R$ = Sc, Y, Ho-Lu) can store large amounts of oxygen at low temperatures[14,15] and are also more refractory than perovskites, indicated by the crystallization temperature from amorphous gel of at least 800 °C.[16] The layered hexagonal manganites are prone to anti-Frenkel defect formation[17] and can also incorporate excess oxygen on interstitial sites, which is possible due to the structure being less close-packed than the perovskite structure.[18−20] Oxygen interstitials move through an interstitialcy mechanism with a low energy barrier compared to those reported for vacancy migration in perovskites,[18,21−23] enabling oxygen transport and exchange at lower temperatures. Remsen and Dabrowski[14] first reported this reversible absorption and release of oxygen for $Dy_{1-x}Y_xMnO_{3+\delta}$ ($0 \leq \delta \leq 0.35$), and similar large excess oxygen values have later been reported for other $RMnO_3$ compositions.[15,24−30]

$RMnO_3$ oxides can crystallize in one of two crystal structures, depending on the ionic radius of the $R^{3+}$ cation; larger cations ($r_R^{3+} \geq r_{Dy}^{3+}$) and a Goldschmidt tolerance factor of $t > 0.855$ favor the orthorhombic perovskite structure with a space group *Pnma*, while the hexagonal $P6_3cm$ structure is preferred for smaller rare earth ions ($r_R^{3+} \leq r_{Ho}^{3+}$) and $t < 0.855$.[31−35] The hexagonal phase is stabilized with respect to the orthorhombic phase both by high temperature and in inert

Received: January 27, 2023
Revised: June 21, 2023
Published: July 24, 2023

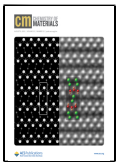

or reducing conditions.[16,31] Crystallizing these materials in an inert atmosphere at high temperatures can thus favor the hexagonal phase for $R^{3+}$ larger than $Ho^{3+}$, and conversely high pressure,[36,37] low temperature,[38] and oxidizing atmosphere favor the orthorhombic phase even for smaller $R^{3+}$. The $P6_3cm$ structure is composed of alternating layers of seven-coordinated $R^{3+}$ and five-coordinated $Mn^{3+}$ in corner-sharing trigonal bipyramids, shown in Figure 1. Interstitial oxygen sites

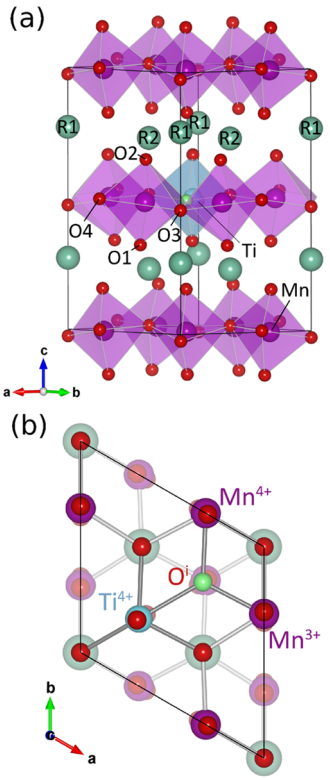


**Figure 1.** (a) Hexagonal crystal structure with a space group $P6_3cm$ of $RMnO_3$ with purple $MnO_5$ bipyramids, blue $Ti^{4+}$ on the Mn-lattice, turquoise $R$ atoms, and green spheres indicating interstitial oxygen. (b) Position of interstitial oxygen in the Mn−O triangular lattice, with the added Ti on the Mn site.

are located between three $Mn^{3+}$ ions in the triangular lattice of $MnO_5$ bipyramids[18] and are charge-compensated by the oxidation of two out of three nearest-neighbor $Mn^{3+}$ to $Mn^{4+}$, as described by eq 1 in the Kröger−Vink notation

$$\frac{1}{2}O_2(g) + 2Mn_{Mn}^{x} \rightarrow O_i'' + 2Mn_{Mn}^{\bullet} \quad (1)$$

For high oxygen contents, interstitial oxygen in the $MnO_5$ layers gives rise to new hexagonal superstructures depending on the value of $\delta$.[15,24,28] Partial substitution of $Y^{3+}$ in $YMnO_3$ with larger $R^{3+}$ such as Tb, Ce, Nd, and Sm improves the oxygen storage and transport properties of these materials, as oxygen absorption and ionic radius of $R^{3+}$ are strongly correlated.[28−30,39−41] Donor dopants like $Ti^{4+}$ on the Mn sublattice can also further increase the maximum storage capacity,[42,43] as oxygen interstitials (eq 2) are energetically favored as a charge compensation mechanism for $Ti^{4+}$ compared to the reduction of $Mn^{3+}$ to $Mn^{2+}$ (eq 3)[27]

$$2\,TiO_2 \rightarrow 2Ti_{Mn}^{\bullet} + 3\,O_O^{x} + O_i'' \quad (2)$$

$$TiO_2 + \frac{1}{2}Mn_2O_3 \rightarrow Ti_{Mn}^{\cdot} + 3\,O_O^{x} + Mn_{Mn}' + \frac{1}{4}O_2(g) \quad (3)$$

For $Ti^{4+}$-doped samples, the value of $\delta$ therefore depends on both the $Ti^{4+}$ concentration and on the fraction of Mn present as $Mn^{4+}$ in the system, as all oxidation of Mn is caused by excess oxygen.[43] The addition of $Ti^{4+}$ also stabilizes the high-temperature $P6_3/mmc$ structure from above the ferroelectric $T_C$ of ∼980 °C[44] to room temperature when cooling down the material in air or oxygen atmosphere.[43] This can be understood as $Ti^{4+}$ and $O_i$ softening the $K_3$ distortion mode driving the ferroelectric transition,[35,45,46] resulting in an expansion of the $ab$-plane, a contraction of the $c$-axis, and a net unit cell expansion. The oxygen absorption of hexagonal manganites can also be tuned by particle size and morphology.[40,47] In general, the catalytic activity for the splitting or recombination of $O_2$ molecules increases with decreasing particle size and increasing surface area.[48,49] Furthermore, the diffusion distance in smaller particles will be shorter and oxygen saturation will occur faster.[50] Both Asakura et al.[47] and Klimkowicz et al.[51] have showed that the oxygen storage and release rate in $YMnO_3$ were enhanced for nanoparticles synthesized using a wet chemical synthesis method, compared to $YMnO_3$ bulk samples.

While the oxygen absorption of prototypical $YMnO_3$ has been studied with respect to aliovalent doping,[27,43] $R$-site substitution,[28−30,39,40] and particle size,[40,47,51] we hypothesize that these effects can be further enhanced by replacing $Y^{3+}$ with $Ho^{3+}$ or $Dy^{3+}$, as both bulk undoped $HoMnO_3$ and $DyMnO_3$ show larger oxygen storage capacity than $YMnO_3$.[14,15,24] Nanocrystalline and donor-doped $HoMnO_3$ and $DyMnO_3$ are hence expected to show improved oxygen storage capacity compared to the corresponding $YMnO_3$-based materials.

Here, we study oxygen absorption and desorption in nanocrystalline hexagonal $RMnO_3$ ($R$ = Y, Ho, Dy), with and without 15% of Ti donor doping. The oxygen storage capacity increases with smaller crystallite size and larger $R^{3+}$ cation from Y through Ho to Dy. Donor doping with $Ti^{4+}$ on the Mn sublattice further increases the oxygen storage capacity and increases the thermal stability of excess oxygen, thereby extending the range of possible operating temperatures. We corroborate the experimental findings with DFT calculations, which show a correlation between the enthalpy of oxidation and the enthalpy of formation for oxygen interstitials for different $R^{3+}$, as well as with lattice parameters. Unit cell expansion is suggested as an explanation for enhanced oxygen storage capacity, regardless of whether it is caused by chemical expansion from larger $R^{3+}$, softening of the ferroelectric mode by $Ti^{4+}$ doping, or by finite size-induced lattice expansion.[16]

## METHODS

**Synthesis.** Undoped and Ti-doped nanocrystalline $RMnO_3$ samples were prepared using a modified citric acid synthesis method previously reported by Bergum et al.[16] For the precursor solutions, $Y(CH_3CO_2)_3{\cdot}xH_2O$ (Sigma-Aldrich), $Ho(CH_3CO_2)_3{\cdot}xH_2O$ (AlfaAesar), $Dy(CH_3CO_2)_3{\cdot}xH_2O$ (AlfaAesar), and $Mn(CH_3CO_2)_3{\cdot}xH_2O$ (Riedel-de-Haën) were each dissolved in a mixture of citric acid (99%, Sigma-Aldrich) and deionized water while stirring at 400 rpm on a hot plate set to 150 °C, resulting in a molar ratio of cation to citric acid of 1:15 for $Y^{3+}$, 1:20 for $Ho^{3+}$, 1:35 for $Dy^{3+}$, and 1:5 for $Mn^{3+}$. For the $Ti^{4+}$ precursor solution, titanium (IV) isopropoxide (TTIP) (Sigma-Aldrich) was added to a mixture of citric acid and deionized water kept at 60 °C under stirring in a molar ratio of 1:6.3. Stoichiometric amounts of cation precursors were mixed with ethylene glycol (EG)


https://doi.org/10.1021/acs.chemmater.3c00189
Chem. Mater. 2023, 35, 5764−5776

(Merck), with a 1:1 molar ratio between EG and citric acid. The final solutions were kept on a hot plate at 150 °C until a viscous gel was formed. This gel was heated to 400 °C and kept for 3 h, before heating to 600 °C at a rate of 200 °C $h^{-1}$ and calcined for 6 h. The resulting amorphous powders were crystallized in a $N_2$ atmosphere at temperatures ranging from 850 to 1000 °C to obtain different crystallite sizes. Ho- and Dy-containing samples were preannealed in 5% $H_2$ in $N_2$ to reduce a fraction of $Mn^{3+}$ to $Mn^{2+}$ prior to crystallization to reduce the effective tolerance factor and favor crystallization of the hexagonal phase.

**Characterization.** X-ray diffraction (XRD) was performed with a Bruker D8 Focus with Cu K$\alpha$ radiation. Lattice parameters and average crystallite size of the powders were determined by Pawley refinement using TOPAS 5.[52] Oxygen stoichiometry was determined by thermogravimetric analysis (TGA) with a Netzsch STA 449C Jupiter with a flowing $O_2$. The samples were first heated to 800 °C at 200 °C $h^{-1}$ and subsequently cooled using rapid rates of 20 °C $min^{-1}$ inside the TGA to purge excess oxygen before measurements. An exception was the Ti-doped $DyMnO_3$ sample that was annealed for 10 h at 600 °C in $N_2$ to avoid rapid oxidation of this material during cooling. TGA was carried out from ambient to 800 °C in an $O_2$ atmosphere with heating and cooling rates of 1 °C $min^{-1}$, except for the Ti-doped $DyMnO_3$ sample, which could be measured at 10 °C $min^{-1}$ due to very fast oxidation kinetics. High-temperature X-ray diffraction (HT-XRD) was performed with a Bruker D8 Advance with Cu K$\alpha$ radiation to investigate the changes in lattice parameters for the samples in $O_2$ and $N_2$ atmospheres. The samples were measured with 25 °C intervals for 35 min at each temperature, first during heating to 550 and 700 °C for undoped and Ti-doped samples, respectively, then during cooling to 50 °C, and thereafter during reheating to 550 or 700 °C, respectively. The samples were finally cooled to room temperature, and the measurements were repeated in a $N_2$ atmosphere. All samples were heated to 500 °C in a $N_2$ atmosphere for 10 h prior to the HT-XRD measurements to purge excess oxygen. The heating and cooling rates were 12 K $min^{-1}$. Tests showed that these nanocrystalline samples did not require any equilibration time for the lattice parameters to stabilize before each measurement. The lattice parameters were determined by Pawley refinements using TOPAS 5.[53,54] Diffractograms of all samples were refined with the $P6_3cm$ space group, except for $DyMnO_3$ where the $Ia\bar{3}$ space group was included to account for the presence of $Dy_2O_3$. The $R3c$ structure[15,24] was used instead of the $P6_3cm$ for the highly oxidized h-$DyMnO_3$ phase in an $O_2$ atmosphere to account for superstructure reflections. The $c$ lattice parameter of the $R3c$ structure ($Z = 18$) was divided by 3 for direct comparison with the $P6_3cm$ ($Z = 6$) structure.

**Computational Details.** All calculations were performed using plane-wave periodic density functional theory (DFT) within the Vienna *ab initio* Simulation Package (VASP)[55−58] and the PBEsol[59] functional. The projector-augmented wave (PAW) method[60] was employed to describe the interactions between the core and the valence electrons using the Y_sv, Dy_3, Ho_3, Er_3, Mn_pv, Ti_sv, and O pseudopotentials supplied with VASP, where all *f*-electrons are kept in the pseudopotential core. A Hubbard U[61] value of 3 eV on Mn 3d was used to account for self-interactions, and a frustrated collinear antiferromagnetic (F-AFM) order was set to approximate the true noncollinear magnetic structure.[18]

Structural optimizations of bulk $RMnO_3$ were performed using a plane-wave energy cutoff of 550 eV and a Γ-centered $k$-point mesh of 4 × 4 × 2 allowing atomic positions, lattice vector, and cell angle and volume to relax until forces on all atoms were less than 0.01 eV $Å^{-1}$. To simulate the effects of oxygen absorption, the formation enthalpy of an oxygen interstitial ($O_i$), corresponding to a very low $\delta$, was calculated using 2 × 2 × 1 supercells (120 + 1 atoms) created from relaxed bulk structures. To simulate a very high $\delta$ value, two $O_i$ were inserted into the 30-atom unit cell, one in each Mn−O layer, giving a stoichiometry of $R_6Mn_6O_{20}$ or $RMnO_{3.33}$ and the cells were fully relaxed. To simulate Ti-doping, 1 out of 24 Mn in a 120-atom supercell was replaced by Ti. This lower concentration (~4%) compared to the experimental (15%) was chosen instead of 1 out of 6 Mn in a 30-atom unit cell (~17%) to avoid artificial Ti-ordering due to periodic boundary conditions.

The enthalpy of formation of a defect ($D$) in a charge-neutral cell was calculated from

$$\Delta H_f(D) = (E^{D,q} - E^H) + \sum_i (E_i + \mu_i) \quad (4)$$

where $E^H$ and $E^{D,q}$ are the total energies of the undoped host and defect supercells, respectively, and $E_i$ and $\mu_i$ correspond to the elemental reference energy of species "$i$" and the associated chemical potential, respectively. Charged supercells were not calculated due to the large nonstoichiometry found in these materials. The enthalpy of oxidation was calculated per mole $O_2$ (g) using eq 5[62]

$$R_6Mn_6O_{18}\ (s) + O_2\ (g) = R_6Mn_6O_{20} \quad (5)$$

## RESULTS

The hexagonal $P6_3cm$ structure is the main phase in all investigated samples, as indicated by the X-ray diffractograms of the as-synthesized materials shown in Figure 2, where the characteristic four distinct reflections of the hexagonal phase are visible between 20 and 34° 2$\theta$. Traces of the orthorhombic *Pnma* phase are found in the Ho-containing samples, indicated with asterisks. The $DyMnO_3$ sample contains ~14% $Dy_2O_3$ as a secondary phase as determined by Rietveld (Supporting Note 1). Preannealing in 5% of $H_2$ atmosphere followed by high-temperature crystallization in $N_2$ favors the hexagonal phase, while a one-step crystallization of samples with $R$ = Dy in $N_2$ gave mainly the competing orthorhombic perovskite phase. The increased background in Ti-doped $YMnO_3$ is caused by the Kapton polyimide film protecting the sample. The (012) and (014) reflections, characteristic of the $P6_3cm$ space group, are less pronounced for the samples containing Ti compared to undoped materials.

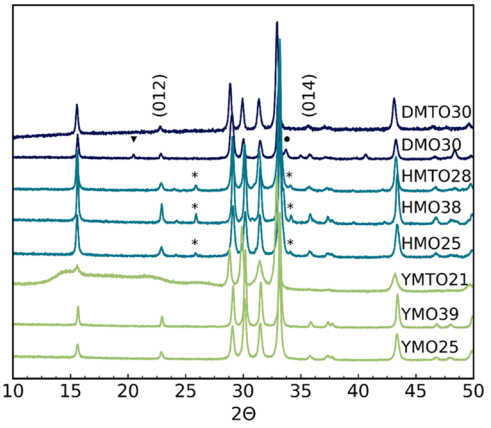


**Figure 2.** X-ray diffractograms of as-synthesized materials with compositions and labels explained in Table 1. The asterisks indicate reflections originating from the competing orthorhombic perovskite phase, the circle indicates the presence of $Dy_2O_3$, while the triangle marks an unidentified reflection.

Refined lattice parameters from the Pawley refinement show that the unit cell dimensions increase with $R$ cation size, with Ti-doping, and with smaller crystallite size, in agreement with previous work.[16,63] All samples are nanocrystalline with average crystallite sizes ranging from 21 to 39 nm. The composition, sample labeling, refined lattice parameters $a$ and $c$, and refined crystallite size for all as-synthesized samples are summarized in Table 1. All samples are labeled based on the composition and


https://doi.org/10.1021/acs.chemmater.3c00189
Chem. Mater. 2023, 35, 5764−5776

Table 1. Composition, Naming, and Pawley Refined Lattice Parameters and Crystallite Sizes of As-Synthesized $RMn_{1-x}Ti_xO_3$ Samples[a]

| composition | crystallite size (nm) | sample name | $a$ (Å) | $c$ (Å) | volume (Å$^3$) | $c/a$ |
|---|---|---|---|---|---|---|
| $YMnO_3$ | 25 ± 1 | YMO25 | 6.141(4) | 11.365(4) | 371.2 | 1.850 |
| $YMnO_3$ | 39 ± 1 | YMO39 | 6.132(5) | 11.351(5) | 369.7 | 1.851 |
| $YMn_{0.85}Ti_{0.15}O_3$ | 21 ± 1 | YMTO21 | 6.194(4) | 11.383(8) | 378.3 | 1.837 |
| $HoMnO_3$ | 25 ± 1 | HMO25 | 6.131(0) | 11.371(0) | 370.2 | 1.854 |
| $HoMnO_3$ | 38 ± 1 | HMO38 | 6.130(1) | 11.361(6) | 369.7 | 1.853 |
| $HoMn_{0.85}Ti_{0.15}O_3$ | 28 ± 1 | HMTO28 | 6.141(8) | 11.400(0) | 372.4 | 1.856 |
| $DyMnO_3$ | 30 ± 1 | DMO30 | 6.162(3) | 11.368(8) | 373.9 | 1.844 |
| $DyMn_{0.85}Ti_{0.15}O_3$ | 30 ± 1 | DMTO30 | 6.199(3) | 11.433(3) | 380.5 | 1.844 |

[a]All samples were refined within the *P*63*cm* space group.

crystallite size. The $a$ and $c$ parameters are similar in value for all of the undoped $RMnO_3$ samples, with $DyMnO_3$ having a subtly larger $a$ parameter, expected from the larger Shannon radius of 7-coordinated Dy (1.027 Å) compared to that of Y (0.96 Å) and Ho (1.015 Å).[64] The samples with the largest refined crystallite sizes are also the same samples that were crystallized at the highest temperatures. The thermal and atmospheric history of all samples is summarized in Table S1. While $Ti^{4+}$ (0.51 Å) is smaller than $Mn^{3+}$ (0.58 Å), the expansion of the unit cell with the addition of $Ti^{4+}$ can be rationalized from the charge-compensating reduction of $Mn^{3+}$ (0.58 Å) to the larger $Mn^{2+}$ (0.75 Å) in a $N_2$ atmosphere.

An essential property of oxygen carriers is the amount of oxygen that can be stored within the material. The maximum oxygen storage capacity of all investigated samples increases with increasing $R$ cation size, decreasing crystallite size, and with the addition of Ti. The changes in oxygen stoichiometry as a function of temperature, measured using thermogravimetry, are shown in Figure 3. All undoped samples (Figure 3a) absorb oxygen during heating starting from about 200 °C, with the absorbed oxygen being stabilized toward increasingly higher temperatures from Y through Ho to Dy. The maximum $\delta$ values also follow the same trend, with Dy having a maximum of $\delta = 0.25$ during cooling (the $Dy_2O_3$ phase in this sample is assumed not to oxidize). The value of $\delta$ compares well with those reported for measurements performed at 1 °C min$^{-1}$ in previous studies.[26,29,51] The smaller crystallite samples, YMO25 and HMO25, display a greater oxygen absorption than the larger crystallite samples, YMO39 and HMO38. The temperature interval where oxygen desorption occurs also becomes increasingly narrower from Y to Ho and especially Dy. A hysteresis in the oxygen content, with a width of up to 100 °C, is observed during cooling and heating, as also reported for other $RMnO_3$.[29,40]

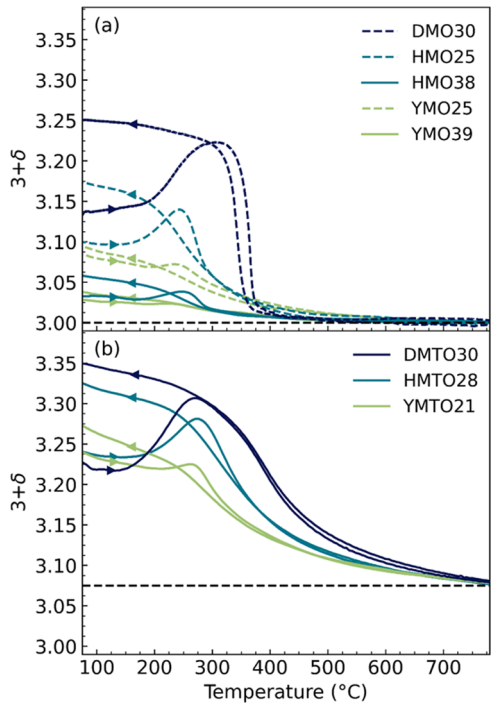


**Figure 3.** Oxygen stoichiometry during heating and cooling in $O_2$ for hexagonal $RMnO_{3+\delta}$ ($R$ = Y, Ho, Dy) for different rare earth cations and crystallite sizes with (a) 0% and (b) 15% Ti donor doping.

For the Ti-doped samples in Figure 3b, the same trend in the maximum value of $\delta$ as a function of $R$ can be seen as for the undoped samples in Figure 3a. The temperature intervals for which oxygen absorption and release occur are also significantly expanded for all of the Ti-doped samples compared to those of the undoped materials. An anticipated plateau at $\delta = 0.075$, corresponding to all Mn present as $Mn^{3+}$, is not reached even at 800 °C, which is the highest temperature measured. Donor doping with $Ti^{4+}$ thus strongly stabilizes $O_i$ to higher temperatures. Compared to the undoped samples displayed in Figure 3a, the maximum excess oxygen for each $RMnO_{3+\delta}$ is also greatly enhanced with Ti substitution, with an increase from $\delta = 0.10$ in YMO25 to 0.27 in YMTO21, from $\delta = 0.17$ in HMO25 to 0.33 in HMTO28, and from $\delta = 0.25$ in DMO30 to 0.35 in DMTO30. The point of maximum excess oxygen during heating is also shifted toward higher temperatures for $R$ = Y, Ho. Some thermal hysteresis in the oxygen content can be seen for the $R$ = Y, Ho samples, while DMTO30 shows little to no hysteresis, suggesting significantly faster oxygen transport kinetics for the latter sample. For calculating $\delta$, a reference point where all Mn is assumed to be $Mn^{3+}$ was chosen at the minimum mass from TGA above 500 °C for each measurement. This point was set to $\delta = 0$ and $\delta = 0.075$ for undoped and Ti-doped samples, respectively, although the Ti-doped samples do not reach a stable plateau even at 800 °C.

X-ray diffractograms for all investigated samples measured with 25 °C increments during cooling in an oxygen atmosphere are displayed in Figure 4. Incorporation of interstitial oxygen causes a unit cell expansion in the $ab$-plane and a unit cell contraction along the $c$-axis, with the latter easily seen from the position of the (004) reflection. For both undoped and Ti-doped Y- and Ho-containing samples, the (004) reflection is shifted toward higher $2\theta$ values, while an


https://doi.org/10.1021/acs.chemmater.3c00189
Chem. Mater. 2023, 35, 5764−5776

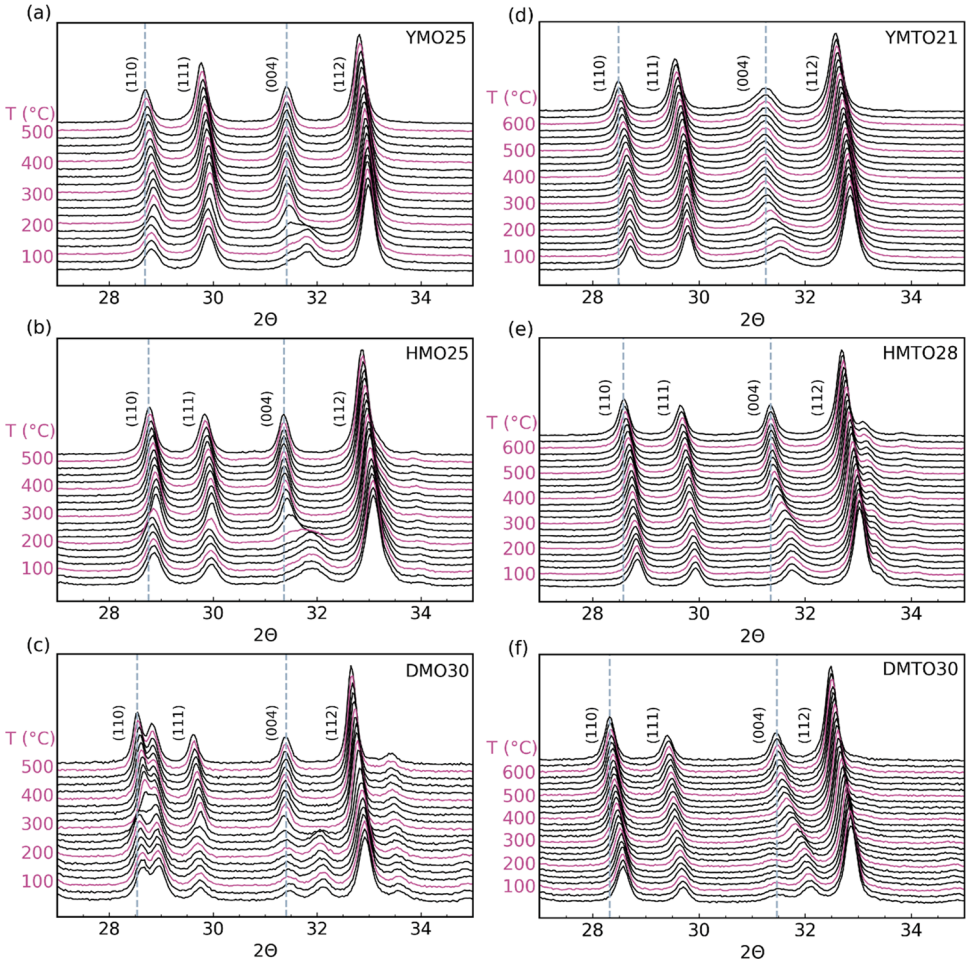


**Figure 4.** X-ray diffractograms of (a) $YMnO_3$, (b) $HoMnO_3$, (c) $DyMnO_3$, (d) $YMn_{0.85}Ti_{0.15}O_3$, (e) $HoMn_{0.85}Ti_{0.15}O_3$, and (f) $DyMn_{0.85}Ti_{0.15}O_3$ measured every 25 °C during cooling in an $O_2$ atmosphere.

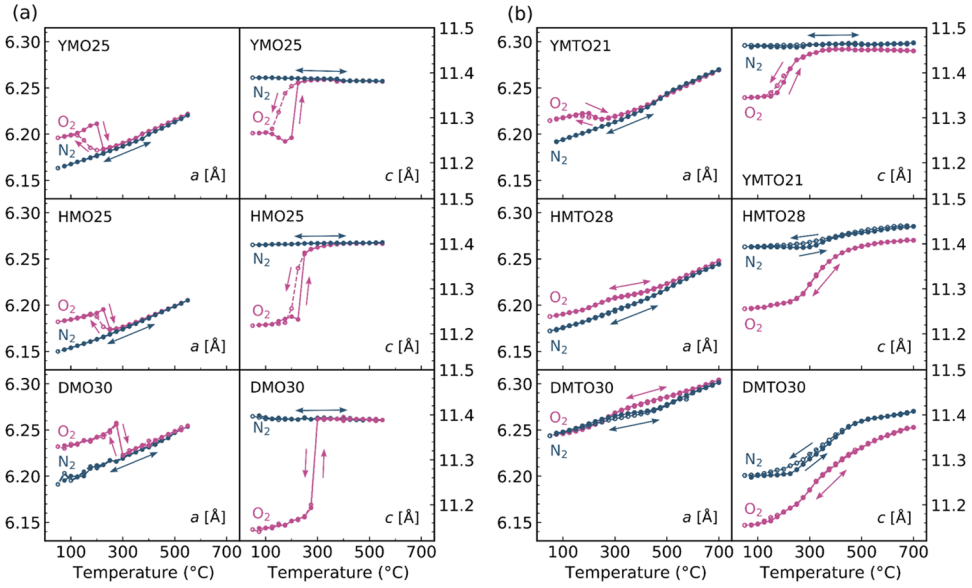


**Figure 5.** Refined lattice parameters *a* and *c* as a function of temperature for (a) undoped and (b) Ti-doped $RMnO_{3+\delta}$ ($R$ = Y, Ho, Dy) in $O_2$ and $N_2$ atmospheres.

additional reflection adjacent to the (004) appears for the DMO30 and DMTO30 samples, as discussed further below.

The (004) reflection at approximately $2\theta = 31.4°$ in all diffractograms is shifted toward higher $2\theta$ angles during oxidation, signifying a contraction of the *c* lattice parameter.



https://doi.org/10.1021/acs.chemmater.3c00189
Chem. Mater. 2023, 35, 5764−5776

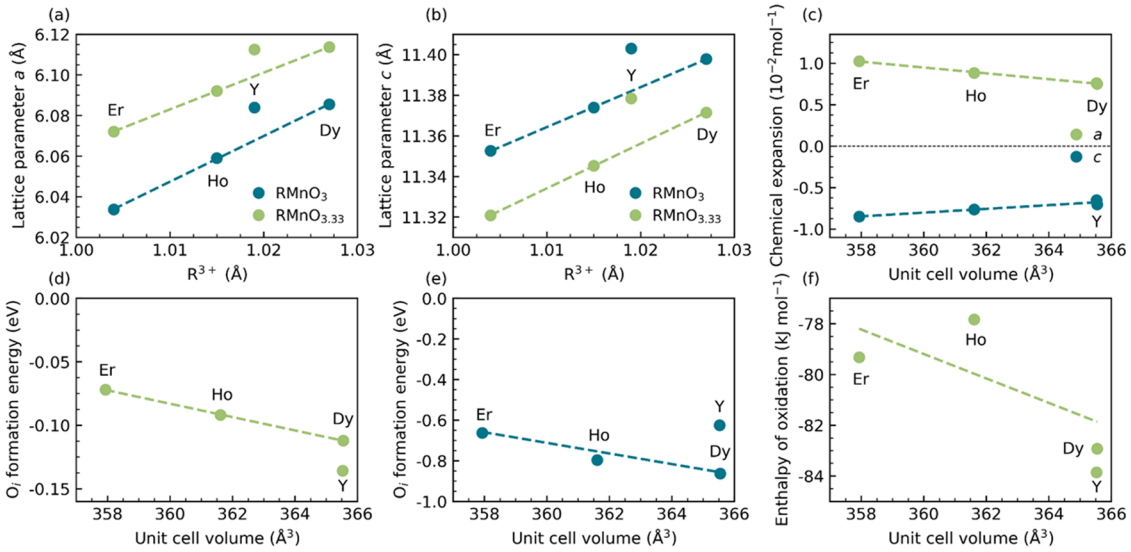


**Figure 6.** (a,b) DFT-calculated lattice parameters of $RMnO_3$ and $RMnO_{3.33}$ ($R_6Mn_6O_{20}$) as a function of the $R^{3+}$ Shannon radius.[64] (c) Chemical expansion as a function of DFT-relaxed stoichiometric unit cell volume. Formation enthalpy for a single $O_i$ point defect in a charge-neutral 120-atom supercell for (d) undoped and (e) Ti-doped materials. (f) Enthalpy of oxidation per $O_2$ molecule for the undoped materials from the reaction $R_6Mn_6O_{18} + O_2$ (g) = $R_6Mn_6O_{20}$. Dashed lines are guides to the eye connecting Er, Ho, and Dy data points (similar pseudopotentials; see the text for an explanation).

This shift in the (004) position becomes more pronounced from $R$ = Y through Ho to Dy for both undoped and Ti-doped samples. The onset temperature for the shift occurs between 150 and 250 °C for undoped samples and at increasingly higher temperatures for the Ti-doped samples from $R$ = Y through Ho and Dy. Ti-doped samples display this (004) position shift over a wider temperature range compared to undoped $RMnO_3$ samples. Both the relative magnitude and the temperature ranges of the (004) shifts agree with the oxygen storage capacities and oxidation onset temperatures observed from the TGA data in Figure 3. Along with the shift of (004), the (110) and (111) reflections are clearly shifted toward lower $2\theta$ angles for Y-containing samples, while this is less pronounced for HMO25 and negligible to subtly opposite for the HMTO28 and Dy-containing samples. For all undoped $R$ = Y and Ho samples, broadening of the (004) reflections is observed upon oxidation, most prominently for HMO25, and this is attributed to inhomogeneous lattice strain caused by oxygen interstitials. For the DMO30 sample, the shift of the (004) reflection is accompanied by new reflections at approximately $2\theta$ = 31.5 and 35° (Figure 4c) and at ∼27 and ∼63° (Figure S2). Similar reflections are also observed for the DMTO30 sample in Figure 4f, with the new reflections gradually appearing at $2\theta$ = 31.5 and 35°, while the original (004) reflection is shifted toward $2\theta$ = 32° during cooling. For the DMO30 sample, the reflection appearing at ∼29° $2\theta$ is due to the $Dy_2O_3$ secondary phase.

The lattice parameters reflect the oxidation of the materials as the incorporation of interstitial oxygen into the $MnO_5$ layers causes significant anisotropic chemical expansion, as already evident from the X-ray diffractograms presented in Figure 4. All samples show shifts in refined lattice parameters (Figure 5) during heating and cooling in an $O_2$ atmosphere, but not in a $N_2$ atmosphere, confirming that the structural changes are caused by the reversible absorption and release of oxygen. The thermal evolution of lattice parameters $a$ and $c$ in $O_2$ and $N_2$ atmospheres is shown for undoped samples in Figure 5a and Ti-doped samples in Figure 5b. For the undoped $RMnO_3$ ($R$ = Y, Ho, Dy) samples, there is an abrupt and large change in both lattice parameters during cooling in $O_2$ from high temperatures as oxygen is absorbed at temperatures between 150 and 300 °C, depending on $R$. The $c$-axis contracts and the $ab$-plane expands over a temperature interval of approximately 100 °C for $R$ = Y, Ho, while for $R$ = Dy, the temperature interval is only ∼25 °C. During heating, the reverse changes take place as oxygen is released, but this occurs over a smaller temperature interval of only ∼25 °C and at slightly higher temperatures than the absorption during cooling for $R$ = Y, Ho, constituting a small hysteresis. For $R$ = Dy, no hysteresis can be seen, which is in accordance with the small thermal hysteresis found from TGA results presented in Figure 3. The temperature ranges of abrupt anisotropic changes in lattice parameters agree with the TGA results presented in Figure 3, confirming oxygen absorption and release as the origin of the anisotropic lattice contraction and expansion, respectively. The magnitude of change of the $c$ parameter in Figure 5a reflects the increasing amount of incorporated $O_i$ from Y to Ho and Dy as shown in Figure 3. As expected, during heating and cooling in $N_2$, no abrupt changes in lattice parameters are observed.

The increased oxygen storage capacity and thermal stability of $O_i$ caused by Ti-doping of $RMnO_3$, evident from the TGA data in Figure 3, are also reflected by the changes in lattice parameters upon heating and cooling in $O_2$ and $N_2$. Both lattice parameters are subtly larger for Ti-doped YMTO21 than for undoped YMO25, indicating a net expansion of the unit cell upon Ti-doping. Lattice parameters $a$ and $c$ for the Ti-doped YMTO21 show qualitatively similar changes in $O_2$ as for the undoped YMO25, but the chemical expansion and contraction are spread out over a wider temperature interval, as expected from the TGA data in Figure 3. YMTO21 also differs from YMO25 by displaying little to no hysteresis upon heating and cooling, and a plateau at $T$ = 350 °C is reached during heating in $O_2$, after which only thermal and no chemical expansion is observed as the sample is heated further. Even at higher temperatures, there is a gap between the $c$ parameter


https://doi.org/10.1021/acs.chemmater.3c00189
Chem. Mater. 2023, 35, 5764−5776

measured in $O_2$ and in $N_2$, indicating that a significant content of absorbed oxygen is stabilized toward higher temperatures by Ti-doping. In a $N_2$ atmosphere, no significant change in lattice parameters can be seen beyond thermal expansion in the *ab*-plane.

In an $O_2$ atmosphere, the HMTO28 and DMTO30 samples behave similarly to the YMTO21 sample. For HMTO28, the sample does not seem to reach a definitive plateau where only thermal expansion is observed during heating, indicating that chemical expansion from interstitial oxygen vacating the structure occurs up to at least $T$ = 700 °C. There is also a visible shift in the *c* parameter during heating and cooling in a $N_2$ atmosphere, suggesting that some incorporation of $O_i$ takes place even in a low $pO_2$ atmosphere (nominally 5.0 purity, $\sim 10^{-4}$ to $10^{-6}$ atm). The gap between the high-temperature values of the *c* parameter in $O_2$ and $N_2$ atmospheres indicates that $O_i$ is stabilized to higher temperatures to a greater extent than in YMTO21. No hysteresis in the lattice parameters can be seen for neither the HMTO28 nor the DMTO30 samples in $O_2$, but there is a visible hysteresis in $N_2$ for the *c* parameter for the former and for both parameters for the latter. For DMTO30, the transition from the highly oxidized state at low temperatures to the low oxidized state at higher temperatures in $O_2$ is gradual and occurs over a broad temperature interval, as can be seen from the *c* parameters in Figure 5b for DMTO30. The *c* parameter differs significantly between $N_2$ and $O_2$ atmospheres even at 700 °C, indicating a significant concentration of $O_i$ in an $O_2$ atmosphere at high temperatures.

For all samples, the expansion and contraction in the *ab*-plane during absorption and desorption of $O_i$ are less significant for the Ti-doped samples, with almost no change in values for HMTO28. For DMTO30, the expansion/contraction in the *a* parameter is reversed during absorption/release in $O_2$ compared to the other samples, as discussed further below. For the latter sample, expansion and contraction are also seen for the *a* parameter in a $N_2$ atmosphere.

The DFT-calculated lattice parameters of $R\mathrm{MnO_3}$ and the "maximally oxidized" model case of $R\mathrm{MnO_{3.33}}$ are strongly correlated with the size of the $R^{3+}$ cation, as shown in Figure 6a. The lattice parameters for $R$ = Dy, Ho, and Er scale close to linearly with cation size, while $R$ = Y has somewhat larger than expected lattice parameters compared to the other $R$, which are 4f rather than 4d elements. The trends in lattice parameters reflect the experimentally observed in Table 1 and Figure 5. Er is included in the computational study as a reference to illustrate the trends with $R^{3+}$ radius as isostructural $\mathrm{ErMnO_3}$ is known to oxidize less readily than the materials studied here.[15] The DFT-calculated 0 K chemical expansion (calculated using eq S2) resulting from incorporating two $O_i$ per 30-atom unit cell is presented in Figure 6c. While the qualitative trends between different $R$ are reproduced, the chemical expansion from DFT is smaller than what was experimentally measured using HT-XRD, shown in Figure 5. This quantitative difference is attributed to the calculations being done for a 0 K situation and with artificially ordered $O_i$ because of periodic boundary conditions. The highly anisotropic chemical expansion, with expansion of the *ab*-plane and contraction of the *c*-axis upon oxidation, becomes smaller for larger $R$. The potential for chemical expansion of the *ab*-plane is smaller for larger $R$ where the lattice parameters are already expanded by the chemical pressure exerted by larger $R$ cations. This trend is supported by the lattice parameters inferred from HT-XRD in $N_2$ and $O_2$ in Figure 5. The contraction of the *c*-axis follows a reduction of the amplitude of the $K_3$ distortion mode[45] driving the ferroelectric transition. Inclusion of $O_i$ leads to a reduction of the $MnO_5$ tilting angle,[18] and the corrugation of the $R$ layer is strongly coupled to this polyhedral tilting through the short and strong $R$2-O4 ionic bond.[46]

The thermodynamic driving force for oxidation is now computationally addressed. For low contents of absorbed oxygen, supercells with stoichiometry $\sim R\mathrm{MnO_{3.04}}$ are used to calculate the enthalpy of formation for a single $O_i$. A clear trend is observed that the incorporation of an $O_i$ defect becomes more energetically favorable for larger $R$ (Figure 6d), although the formation enthalpies are of very similar magnitude. The formation enthalpies are plotted as a function of DFT-relaxed unit cell volume for stoichiometric materials. Compared to the undoped compounds, Ti-doping strongly stabilizes $O_i$ formation by 0.49−0.75 eV and more for larger than smaller $R$ (Figure 6e). A negative enthalpy of formation for a point defect is uncommon and depends strongly on the choice of oxygen chemical potential (here: oxidizing limit, $\mu_O$ = −5.14 eV) and on the choice of Hubbard U as a larger U will favor occupation of transition-metal d-states and thus energetically disfavor oxidation. However, a negative enthalpy of oxidation is necessary to give a negative Gibbs free energy of oxidation, as experimentally observed, as the oxidation reaction where $O_2$ molecules are consumed must have a large negative entropy of reaction.

To assess the thermodynamic driving force for "full" oxidation, the enthalpy of oxidation is calculated per $O_2$ molecule, as shown in Figure 6f. Following the arguments above, the enthalpies of oxidation are negative as expected and this is the driving force for the oxidation reaction. The calculated values for different $R$ show the same spread as the $O_i$ formation enthalpies in Figure 6d, with values corresponding to −78 to −84 kJ $\mathrm{mol^{-1}}$, but do not follow the same simple trend with the $R^{3+}$ radius. This suggests that thermodynamics alone cannot explain the experimentally observed differences in oxygen storage capacity for different $R$, as discussed further below.

## DISCUSSION

Nanocrystalline samples show greater oxygen storage capacity than bulk material cooled at the same rate. As reducing the crystallite size does not increase the thermal stability of absorbed oxygen, the observed increase in capacity is mainly attributed to shorter diffusion distances, which allow the exchange of oxygen with the atmosphere down to lower temperatures.[50] A larger surface area will also improve the oxygen surface exchange kinetics, but it is not known whether bulk diffusion or surface exchange is the rate-limiting factor for oxygen absorption and desorption in these materials.

**Ti-Doping and Application Potential.** As evident from TGA (Figure 3) and HT-XRD (Figures 4 and 5), Ti-doping increases both the measured maximum oxygen absorption capacity and the thermal stability of absorbed oxygen compared to undoped materials, following eq 2. As a donor dopant, $Ti^{4+}$ on $Mn^{3+}$ sites increases the electrostatic attraction for $O_i$ in the position illustrated in Figure 1 and only one $Mn^{3+}$ needs to be oxidized instead of two for charge compensation in the vicinity of $Ti^{4+}$. Furthermore, as eq 3 describes, a $Ti^{4+}$ donor dopant that is not charge-compensated by an $O_i$ leads to a reduction of $d^4$ $Mn^{3+}$ to $d^5$ $Mn^{2+}$. In the trigonal bipyramidal crystal field splitting, this implies occupation of the higher-energy Mn $3d_{z^2}$ orbital,[65] creating a strong thermodynamic


https://doi.org/10.1021/acs.chemmater.3c00189
Chem. Mater. 2023, 35, 5764−5776

driving force for the absorption of $O_i$ (eq 2) to avoid the reduction of $Mn^{3+}$ to $Mn^{2+}$ (eq 3) and furthermore a stabilization of absorbed excess oxygen to higher temperatures. This interpretation is supported by the present and previous[66] DFT calculations. Increasing the stability of absorbed oxygen to higher temperatures may increase the kinetics of pressure swing separation of oxygen from air, but the broad temperature interval of oxygen absorption for Ti-doped samples is less ideal for temperature-swing separation. Ti-doping also reduces thermal hysteresis in oxygen absorption (Figure 3), and further studies are needed to understand the kinetics of bulk mass transport and oxygen surface exchange to identify possible rate-limiting steps. In contrast, for undoped materials, $R$ = Dy gives both the highest oxygen storage capacity and thermal stability as well as a narrow temperature interval of oxidation, which is preferable for temperature-swing separation of oxygen from air.

**Chemical and Thermal Expansion.** The large differences in oxygen absorption for the different $R$ cations agree with literature reports[14,15,24−26] on undoped materials. Y-containing samples display the smallest absorption and Dy-samples the largest, following a trend in Shannon radii where larger $R^{3+}$ cations give larger oxygen absorption, although no significant difference in lattice parameters was observed experimentally between $YMnO_3$ and $HoMnO_3$ with similar crystallite sizes (Table 1). The change in the $c$ lattice parameter upon oxygen absorption and release is correlated with the amount of oxygen absorbed, while a corresponding trend is not seen for the $ab$-plane. The larger $R^{3+}$ cations are believed to expand the $ab$-plane and thus reduce the electrostatic repulsion between $O_i$ and regular planar O3 and O4 and therefore thermodynamically favor oxygen absorption. For initial oxygen absorption for low $\delta$ values, this hypothesis is supported by the DFT-calculated $O_i$ formation enthalpies in Figure 6d, while the situation is likely to become more complex upon gradual filling of vacant $O_i$ sites as no simple trend is observed for the enthalpy of oxidation in Figure 6f. Following the unit cell expansion hypothesis, Ti-doping also expands the $ab$-plane (Table 1) despite the smaller Shannon radius of $Ti^{4+}$ compared to $Mn^{3+}$, and this expansion is attributed to the partial rectification of tilted corner-sharing $MnO_5$ bipyramids.[35]

Anisotropic chemical expansion (CE) and thermal expansion (TE) are summarized in Figure 7 where the thermal expansion (Figure 7a) is inferred from HT-XRD data collected upon cooling in a $N_2$ atmosphere. Details on how CE and TEC were calculated are given in the Supporting Information. Any "excess" expansion or contraction of the lattice parameter $i$ in an $O_2$ atmosphere upon cooling is attributed to chemical expansion (Figure 7b) and calculated from $\mathrm{CE} = \frac{1}{i_o}\left(\frac{\Delta i}{\delta}\right)$, with $\Delta\delta$ taken from the TGA measurements presented in Figure 3. Estimated error bars are smaller than the symbol size.

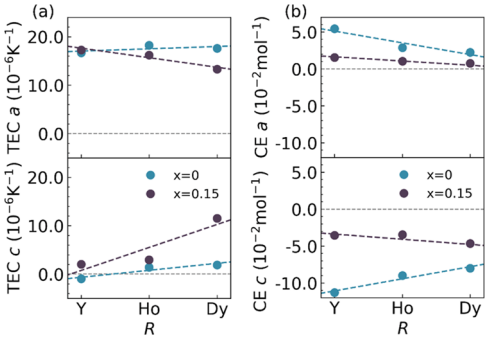


**Figure 7.** Thermal expansion coefficients (TECs) and chemical expansion (CE) for $RMn_{1-x}Ti_xO_3$ samples.

Thermal expansion is more anisotropic for larger $R$ and more isotropic for Ti-doped than undoped samples. In contrast, chemical expansion is more anisotropic for smaller $R$ and generally much smaller for Ti-doped samples. Smaller CE for larger $R$ is qualitatively in agreement with the DFT results in Figure 6b but with larger values than the calculated. A quantitative comparison between 0 K calculation and finite temperature measurements is difficult, also because the chemical expansion of transition-metal oxides is sensitive to computational parameters.[67] As Ti-doping already expands the $ab$-plane by partly rectifying the $MnO_5$ tilting,[43] the smaller CE observed for Ti-doped samples may be rationalized from the $ab$-plane already being more expanded prior to oxygen absorption compared to undoped samples. Correspondingly, the chemical contraction of the $c$-axis is much smaller for Ti-doped samples and of similar magnitude for all $R$. A possible reason for the smaller chemical expansion of Ti-doped samples is that the $ab$-plane is already expanded before oxygen absorption occurs because of the mentioned untilting of the $MnO_5$ bipyramids, which both Ti-doping and $O_i$[18] incorporation induce. With the already partly rectified bipyramids, the expansion caused by the incorporation of $O_i$ may then be counteracted and even dominated by the considerably smaller radius of $Mn^{4+}$ (0.46 Å, CN = 5, interpolated from CN = 4,6) compared to $Mn^{3+}$ (0.58 Å).[64] Ti-doped $HoMnO_3$ (HMTO30) and particularly Ti-doped $DyMnO_3$ (DMTO30) display nonlinearity in lattice parameters also in a $N_2$ atmosphere (Figure 5), in contrast with the other samples, which is likely an effect of trace amounts of oxygen in 5.0 $N_2$ gas.

Chemical expansion is most easily visualized from the (004) reflection (Figure 4). Pronounced broadening of the (004) reflection upon oxidation for the Y- and Ho-containing samples indicates structural disorder and inhomogeneous lattice strain caused by the incorporation of $O_i$. This reflection broadening is not as prominent in the DMO30 sample, but here a new reflection appears adjacent to the (004) reflection. This apparent splitting of the (004) reflection has been attributed to a new hexagonal phase named Hex1 with the space group $R3c$, which has been reported at higher oxygen content ($\delta > 0.28$).[15,24] In this superstructure, the $c$-axis of the original unit cell is tripled, with the appearance of two reflections at ∼31.5° $2\theta$ and ∼32° $2\theta$ having Miller indices (1010) and (0012), respectively. Even if the DMO30 sample has a maximum oxygen content of $\delta$ = 0.25 from TGA (Figure 3), the appearance of this reflection could stem from a Hex1 phase, even though this structure is usually observed for higher $\delta$. The absence of a distinct extra reflection for the other samples with $\delta > 0.28$, HMTO28 and DMTO30, implies a more disordered structure or distribution of $O_i$.

**Thermodynamic Model.** We now address the thermodynamics of oxidation of hexagonal manganites. While a variation in the maximum $\delta$ of 0.33−0.35 in $RMnO_{3+\delta}$ has been reported for cooling in an $O_2$ atmosphere[14,24,68] (even larger values of up to 0.45 have also been reported for $Y_{0.7}Tb_{0.3}MnO_{3+\delta}$[28]), we here use $\delta$ = 0.33 to approximate the maximally oxidized phase as the stoichiometry $R_3Mn_3O_{10}$. We note that only the HMTO and DMTO materials reached comparable values for $\delta$ from


https://doi.org/10.1021/acs.chemmater.3c00189
Chem. Mater. 2023, 35, 5764−5776

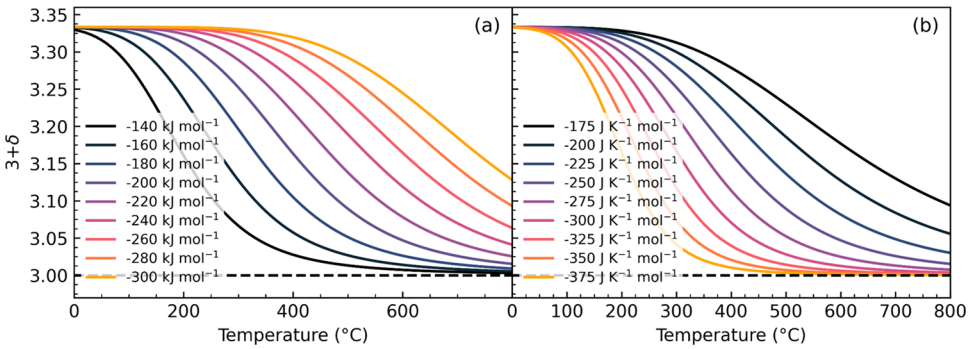


**Figure 8.** Temperature-dependent oxygen stoichiometry in $R\mathrm{MnO}_{3+\delta}$ in a pure $O_2$ atmosphere from eq 10 with (a) variable $\Delta_{ox}H^0$ with $\Delta_{ox}S^0$ fixed to −250 J K$^{-1}$mol$^{-1}$ and (b) variable $\Delta_{ox}S^0$ with $\Delta_{ox}H^0$ fixed to −200 kJ mol$^{-1}$.

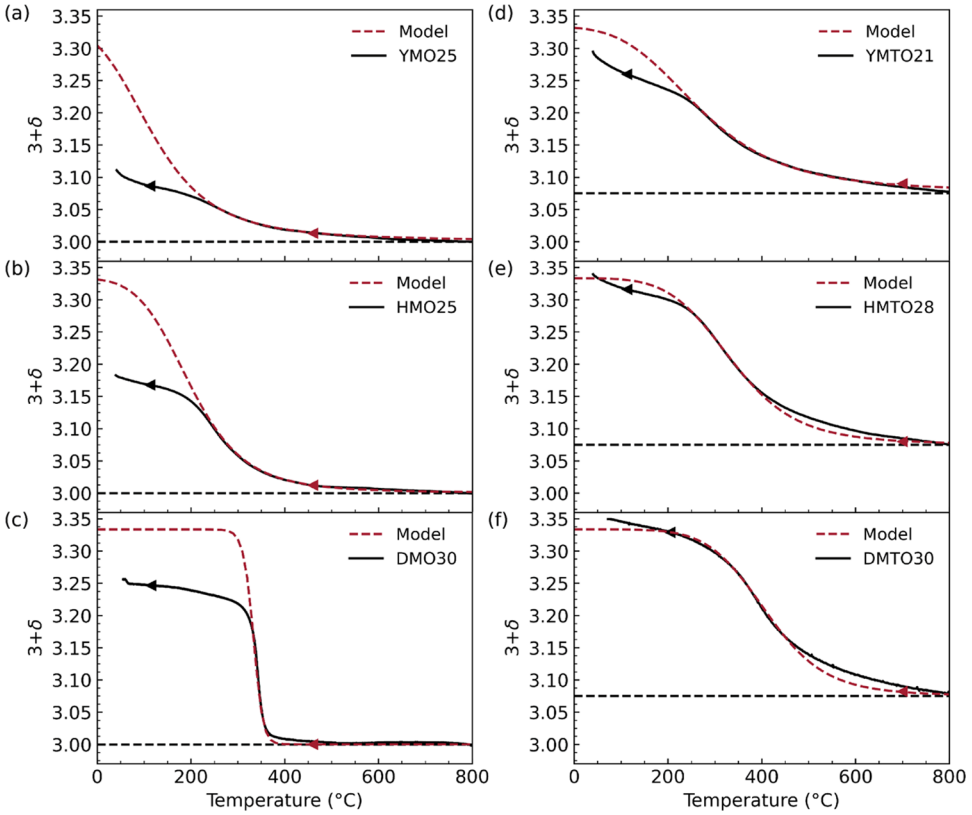


**Figure 9.** Fitted oxygen stoichiometry as a function of temperature with $pO_2$ set to 1.0 is shown as solid lines; experimental data are shown as dashed lines for nanocrystalline (a) $\mathrm{YMnO}_{3+\delta}$, (b) $\mathrm{HoMnO}_{3+\delta}$, (c) $\mathrm{DyMnO}_{3+\delta}$, (d) $\mathrm{YMn}_{0.85}\mathrm{Ti}_{0.15}\mathrm{O}_{3+\delta}$, (e) $\mathrm{HoMn}_{0.85}\mathrm{Ti}_{0.15}\mathrm{O}_{3+\delta}$, and (f) $\mathrm{DyMn}_{0.85}\mathrm{Ti}_{0.15}\mathrm{O}_{3+\delta}$. Horizontal dashed lines correspond to all Mn present as $Mn^{3+}$ and thus $\delta = 0$ for (a−c) and $\delta = 0.075$ for (d−f).

TGA with a cooling rate of 1 °C min$^{-1}$ (Figure 3). Following these assumptions, complete oxidation of $R\mathrm{MnO}_3$ to $R\mathrm{MnO}_{3+\delta}$ can be described by eq 6

$$2\ R_3\mathrm{Mn}_3^{3+}\mathrm{O}_9 + \mathrm{O}_2(g) \rightleftarrows 2\ R_3\mathrm{Mn}^{3+}\mathrm{Mn}_2^{4+}\mathrm{O}_{10} \quad (6)$$

To discuss the thermodynamics of the oxidation reaction, the solid solution model by Bakken et al.[69] for the formation of oxygen vacancies in a perovskite, $\mathrm{ABO}_{3-\delta}$, is adapted, utilizing that oxidation of $R\mathrm{MnO}_{3+\delta}$ from $R\mathrm{MnO}_{3.00}$ with $\delta = 0.00$ to $R\mathrm{MnO}_{3.33}$ with $\delta = 0.33$ is analogous to oxidation of $\mathrm{ABO}_{2.50}$ brownmillerite to perovskite $\mathrm{ABO}_{3.00}$. Equivalent to $R\mathrm{MnO}_3$ incorporating "excess" $O_i$, unfilled interstitial sites in $R_3\mathrm{Mn}_3\mathrm{O}_{10-\delta}$ can be regarded as oxygen vacancies where stoichiometric $R\mathrm{MnO}_3$ is written as $R_3\mathrm{Mn}_3\mathrm{O}_9$. The formation of oxygen vacancies, $V_O^{\bullet\bullet}$, in $R_3\mathrm{Mn}_3\mathrm{O}_{10}$ is shown in the Kroger−Vink notation in eq 7

$$2\mathrm{O}_O^x + 4\mathrm{Mn}_{Mn}^x \leftrightarrow 2V_O^{\bullet\bullet} + 4\mathrm{Mn}_{Mn}' + \mathrm{O}_2(g) \quad (7)$$

The equilibrium constant, $K$, for the defect formation in eq 7 is given by

$$K = \frac{[V_O^{\bullet\bullet}]^2[\mathrm{Mn}_{Mn}']^4}{[\mathrm{O}_O^x]^2[\mathrm{Mn}_{Mn}^x]^4}\cdot pO_2 \quad (8)$$

The Gibbs energy of formation for any given configuration of $R\mathrm{MnO}_{3+\delta}$ can now be expressed from a reaction between $R_3\mathrm{Mn}_3\mathrm{O}_9$ and $R_3\mathrm{Mn}_3\mathrm{O}_{10}$


https://doi.org/10.1021/acs.chemmater.3c00189
Chem. Mater. 2023, 35, 5764−5776

$$\Delta_f G_{c(R_3Mn_3O_{10-\delta})} = (2-2\delta)\Delta_f G^0_m(R_3Mn_3O_{10}) + 2\delta\Delta_f G^0_m(R_3Mn_3O_9) \quad (9)$$

Ideal solution is assumed in eq 9, implying no interactions between oxygen interstitials. By expressing the site fractions $[i]$ in eq 8 as a function of oxygen vacancies, $\delta$, the partial pressure of oxygen can be described by eq 10

$$\log pO_2 = \left(\frac{1}{RT\ \ln\ 10}\right)[2\Delta_f G^0(R_3Mn_3O_{10}) - 2\Delta_f G^0(R_3Mn_3O_9)] + 4[\log(2-2\delta) - \log(2\delta)] - 2\log\left(\frac{\delta}{10-\delta}\right) \quad (10)$$

To model the oxygen stoichiometry of $RMnO_{3+\delta}$ measured by TGA as a function of temperature in a pure $O_2$ atmosphere, $pO_2$ in eq 10 is set to 1.0 and eq 11 expresses the Gibbs energy of oxidation

$$\Delta_{ox}G^0 = 2\Delta_f G^0(R_3Mn_3O_{10}) - 2\Delta_f G^0(R_3Mn_3O_9) = \Delta_{ox}H^0 - T\Delta_{ox}S^0 \quad (11)$$

for the oxidation reaction in eq 6. Before fitting the experimental TGA data, we first illustrate how the enthalpy and entropy of oxidation influence the temperature-dependent $\delta$ in Figure 8 with a range of values chosen from the experimental work on related ternary transition-metal perovskites.[69−71]

The plots of the thermodynamic model show that an increasingly negative $\Delta_{ox}H^0$ (Figure 8a) stabilizes absorbed interstitial oxygen to higher temperatures, counteracting the positive $T\Delta_{ox}S^0$ contribution to $\Delta_{ox}G^0$. This implies that $\Delta_{ox}H^0$ should become increasingly negative for larger $R$,[14,15,24] e.g., by substituting Y in $YMnO_3$ with larger $R^{3+}$ cations like $Tb^{3+}$,[28,30] $Ho^{3+}$, and $Dy^{3+}$, and upon donor doping with $Ti^{4+}$ (this study) and $Zr^{4+}$,[27] in qualitative agreement with the present and previous experimental observations. The effect of increasingly negative $\Delta_{ox}S^0$ (Figure 8b) is to make the temperature interval of complete oxidation narrower, simultaneously shifting both the onset and completion of oxidation to lower temperatures. We note that the DFT-calculated $\Delta_{ox}H^0$ cannot quantitatively explain the experimental observations as the calculated values are too small and would predict oxidation at lower temperatures than experimentally observed, unless a correspondingly small $\Delta_{ox}S^0$ is used to compensate. Furthermore, attempts to fit the TGA data to the thermodynamic model with DFT-calculated $\Delta_{ox}H^0$ and $\Delta_{ox}S^0$ values below 150 J $K^{-1}mol^{-1}$ give a much broader temperature interval of oxidation than that observed experimentally. The trends between the different materials studied were, however, reproduced by the DFT results in Figure 6d−f.

As this is a thermodynamic model, kinetics and ergodicity[50] are ignored, and in real h-$RMnO_3$ materials, oxygen becomes immobile and effectively frozen in the lattice below ∼150 to 200 °C.[14,15,24,26] While the thermodynamic model implicitly assumes that a maximum oxygen content of $\delta = 0.33$ is always reached; $\delta$ measured by TGA deviates from the thermodynamic model at lower temperatures where the available thermal energy is insufficient for thermodynamic equilibrium to be reached. For this reason, we also only fit TGA data upon cooling as the material starts in equilibrium at higher temperatures and because it is difficult to quantify at what temperature ergodicity is broken.

Fits of the thermodynamic model to experimental data from TGA are presented in Figure 9 where $\Delta_{ox}H^0$ and $\Delta_{ox}S^0$ were used as fitting parameters. For fitting the data of Ti-containing samples, the minimum value of $\delta$ in eq 10 was adjusted to 0.075. At higher temperatures, where the materials are in equilibrium, the model fits the experimental data for all undoped samples well. The deviation between the model and measured data starts at progressively higher values of $\delta$ for $R$ = Y, Ho, and Dy, reflecting the difference in oxygen storage capacity for different $R$. The temperature onset of deviation can be regarded as the temperature where ergodicity is broken, and this occurs at ∼250 °C for $R$ = Y and Ho and at ∼325 °C for $R$ = Dy. For Ti-doped samples, shown in panels (d−f) in Figure 9, the deviation between model and data at lower temperatures is less significant due to the larger maximum $\delta$ measured for these samples. At temperatures over ∼450 °C, the model predicts a lower $\delta$ for $R$ = Ho, Dy than what has been measured. Possible reasons for this deviation are that in the present model with a maximum $\delta$ of 3.33, neither surface adsorption nor possible oxidation of $Dy^{3+}$ to $Dy^{4+}$[72] is considered. Given that the thermodynamic model assumes ideal solution with no interactions between absorbed $O_i$ and thus a $\delta$-independent $\Delta_{ox}H^0$ and $\Delta_{ox}S^0$, the fitted values of these thermodynamic quantities must be examined further and are summarized in Table 2. Fitted values for $\Delta_{ox}H^0$ and $\Delta_{ox}S^0$ are of similar magnitude for both undoped and Ti-doped $R$ = Y and Ho and are comparable to previously reported values for related perovskite materials.[70,71,73,74] The DFT-calculated $\Delta_{ox}H^0$ values only give a reasonable match for the undoped $YMnO_3$ and apparently underestimates the $\Delta_{ox}H^0$ values for the other materials studied here. The fitted values for $\Delta_{ox}S^0$ for the Ti-doped for $R$ = Y, Ho samples are slightly larger compared to those of the undoped samples. The values for the Ho-sample are somewhat larger than for that based on Y, reflecting the higher temperature of oxidation for the Ho-sample (trends are illustrated in Figure 8). The same trend can be seen for all Ti-doped samples, where the fitted values increase for increasing $R$ cation size. The fitted values for $DyMnO_{3+\delta}$ are, in contrast, unphysically large but necessary to fit the measured data to the applied model, which is based on the ideal solution. Clearly, an ideal solution model with $\delta$-independent $\Delta_{ox}H^0$ and $\Delta_{ox}S^0$ cannot describe the oxidation of $DyMnO_{3+\delta}$ as it occurs over a too narrow temperature interval. Following the preceding discussion of the role of *ab*-plane expansion, it is possible that partial oxidation strongly facilitates further oxidation of $DyMnO_{3+\delta}$ as $O_i$ causes chemical

**Table 2. Entropy and Enthalpy of Oxidation of $RMn_{1-x}Ti_xO_{3+\delta}$ ($R$ = Y, Ho, Dy) Used for Fitting the Ideal Solid Solution Model to the Experimental Data from TGA Measurements**

| composition | sample name | $\Delta_{ox}S^0$ (J $K^{-1}mol^{-1}$) | $\Delta_{ox}H^0$ (kJ $mol^{-1}$) |
|---|---|---|---|
| $YMnO_{3+\delta}$ | YMO25 | −200 | −97.5 |
| $HoMnO_{3+\delta}$ | HMO25 | −290 | −160 |
| $DyMnO_{3+\delta}$ | DMO30 | −2400 | −1485 |
| $YMn_{0.85}Ti_{0.15}O_{3+\delta}$ | YMTO21 | −195 | −135 |
| $HoMn_{0.85}Ti_{0.15}O_{3+\delta}$ | HMTO28 | −315 | −225 |
| $DyMn_{0.85}Ti_{0.15}O_{3+\delta}$ | DMTO30 | −400 | −310 |


https://doi.org/10.1021/acs.chemmater.3c00189
Chem. Mater. 2023, 35, 5764−5776

expansion of the *ab*-plane, possibly reducing $O-O_i$ repulsion and thus making $\Delta_{ox}H^0$ more negative, up to a value of $\delta$ where $O_i-O_i$ repulsion is expected to dominate and make $\Delta_{ox}H^0$ less negative. This anticipated $\delta$-dependent variation of $\Delta_{ox}H^0$ is not captured by an ideal solution model where defect−defect interactions are ignored. Different diffusion kinetics at different oxidation temperatures are also not accounted for in a purely thermodynamic model, and this is expected to affect the temperature interval of oxidation measured upon a finite cooling rate (here 1 °C $min^{-1}$). Finally, the collective ionic motion[75] may also contribute to the narrow temperature interval of oxidation observed for $DyMnO_{3+\delta}$, especially given the inherently cooperative nature of the interstitialcy mechanism established for migration oxygen ions,[17,18] but the longer-range cooperative ionic motion has not yet been studied for finite oxygen hyperstoichiometry in hexagonal manganites.

## CONCLUSIONS

The oxygen storage capacity of nanocrystalline hexagonal $RMnO_{3+\delta}$ has been observed by thermogravimetric analysis (TGA) to increase with increasing size of the $R^{3+}$ cation and with 15% of Ti-doping of the Mn sublattice. The thermal stability of absorbed oxygen, signified by the onset temperature for absorption upon cooling, was found to be ∼75 °C higher for *R* = Dy than for *R* = Y and Ho, in agreement with previous studies of bulk materials. Ti-doping stabilizes absorbed oxygen to higher temperatures, and Ti-doped samples oxidize over a wider temperature range than undoped samples. High-temperature X-ray diffraction in $O_2$ and $N_2$ showed that the chemical expansion from oxygen absorption is smaller for larger *R* in undoped samples and significantly smaller for Ti-doped samples than for undoped. Super-reflections emerge upon oxidation of $DyMnO_3$ and $DyMn_{0.85}Ti_{0.15}O_3$, signifying the appearance of a new ordered phase, while only shifts in the Bragg reflections were observed for the other samples studied by HT-XRD. Density functional theory (DFT) calculations support the experimental observations of chemical expansion, predict a correlation between the initial thermodynamic driving force for oxidation at low values of $\delta$ and the size of $R^{3+}$, and show that Ti-doping strongly stabilizes absorbed interstitial oxygen. A trend in the enthalpy of oxidation from $\delta$ = 0 to $\delta$ = 0.33 with *R* could not be inferred from the DFT calculations, suggesting that the process in real materials is complex and involves both thermodynamic and kinetic factors. A thermodynamic model for oxidation was derived assuming ideal solution, and this model could be fitted to TGA data for *R* = Y and Ho with reasonable values for the enthalpy and entropy of reduction but not for *R* = Dy, where the narrow temperature interval of oxidation yields unphysically large values for these thermodynamic quantities. The limitations of the ideal solution thermodynamic model are discussed with respect to the microscopic mechanisms involved in oxygen absorption in hexagonal manganites.

## ASSOCIATED CONTENT

### Supporting Information

The Supporting Information is available free of charge at https://pubs.acs.org/doi/10.1021/acs.chemmater.3c00189.

Thermal and atmospheric history of samples, high-temperature X-ray diffractograms, and thermal and chemical expansion calculations (PDF)

## AUTHOR INFORMATION


### Corresponding Author

**Sverre M. Selbach** − *Department of Materials Science and Engineering, NTNU Norwegian University of Science and Technology, NO-7491 Trondheim, Norway;* orcid.org/0000-0001-5838-8632; Email: selbach@ntnu.no

### Authors

**Frida Hemstad Danmo** − *Department of Materials Science and Engineering, NTNU Norwegian University of Science and Technology, NO-7491 Trondheim, Norway*

**Benjamin A. D. Williamson** − *Department of Materials Science and Engineering, NTNU Norwegian University of Science and Technology, NO-7491 Trondheim, Norway;* orcid.org/0000-0002-6242-1121

**Didrik R. Småbråten** − *Department of Materials Science and Engineering, NTNU Norwegian University of Science and Technology, NO-7491 Trondheim, Norway*

**Nikolai H. Gaukås** − *Department of Materials Science and Engineering, NTNU Norwegian University of Science and Technology, NO-7491 Trondheim, Norway*

**Elise R. Østli** − *Department of Materials Science and Engineering, NTNU Norwegian University of Science and Technology, NO-7491 Trondheim, Norway*

**Tor Grande** − *Department of Materials Science and Engineering, NTNU Norwegian University of Science and Technology, NO-7491 Trondheim, Norway;* orcid.org/0000-0002-2709-1219

**Julia Glaum** − *Department of Materials Science and Engineering, NTNU Norwegian University of Science and Technology, NO-7491 Trondheim, Norway;* orcid.org/0000-0002-4871-4438

Complete contact information is available at: https://pubs.acs.org/10.1021/acs.chemmater.3c00189


### Notes

The authors declare no competing financial interest.

## ACKNOWLEDGMENTS

The authors thank Kristin Høydalsvik Wells for help with the HT-XRD measurements and MSc Tormod Østmoe for preparing the $DyMnO_3$ amorphous powder. Financial support from the Research Council of Norway for BADW and DRS through projects 275810 and 275139, respectively, is acknowledged. Computational resources were provided by Sigma2—The National Infrastructure for High-Performance Computing and Data Storage in Norway—through project NN9264K. Financial support from the NTNU Norwegian University of Science and Technology is acknowledged.

## REFERENCES

(1) Rydén, M.; Lyngfelt, A.; Mattisson, T.; Chen, D.; Holmen, A.; Bjørgum, E. Novel Oxygen-Carrier Materials for Chemical-Looping Combustion and Chemical-Looping Reforming; $La_xSr_{1-x}Fe_yCo_{1-y}O_{3-d}$ Perovskites and Mixed-Metal Oxides of NiO, $Fe_2O_3$ and $Mn_3O_4$. *Int. J. Greenhouse Gas Control* **2008**, *2*, 21−36.

(2) Yao, H. C.; Yao, Y. F. Y. Ceria in Automotive Exhaust Catalysts. I. Oxygen Storage. *J. Catal.* **1984**, *86*, 254−265.

(3) Kim, C. H.; Qi, G.; Dahlberg, K.; Li, W. Strontium-Doped Perovskites Rival Platinum Catalysts for Treating $NO_x$ in Simulated Diesel Exhaust. *Science* **2010**, *327*, 1624−1627.

(4) Protasova, L.; Snijkers, F. Recent Developments in Oxygen Carrier Materials for Hydrogen Production via Chemical Looping Processes. *Fuel* **2016**, *181*, 75−93.
(5) Yang, Z.; Lin, Y. S.; Zeng, Y. High-Temperature Sorption Process for Air Separation and Oxygen Removal. *Ind. Eng. Chem. Res.* **2002**, *41*, 2775−2784.
(6) Fornasiero, P.; Graziani, M.; Kaspar, J. Use of $CeO_2$-Based Oxides in the Three-Way Catalysis. *Catal. Today* **1999**, *50*, 285−298.
(7) Chen, B.-Y.; Chang, H. L. R. Development of Low Temperature Three-Way Catalysts for Future Fuelefficient Vehicles. *Johnson Matthey Technol. Rev.* **2015**, *59*, 64−67.
(8) Guntuka, S.; Banerjee, S.; Farooq, S.; Srinivasan, M. P. A- and B-Site Substituted Lanthanum Cobaltite Perovskite as High Temperature Oxygen Sorbent. 1. Thermogravimetric Analysis of Equilibrium and Kinetics. *Ind. Eng. Chem. Res.* **2008**, *47*, 154−162.
(9) Miura, N.; Ikeda, H.; Tsuchida, A. $Sr_{1-x}Ca_xFeO_{3-\delta}$ as a New Oxygen Sorbent for the High-Temperature Pressure-Swing Adsorption Process. *Ind. Eng. Chem. Res.* **2016**, *55*, 3091−3096.
(10) Magnone, E.; Kim, J. R.; Park, J. H. Effect of Synthesis Method on Oxygen Adsorption/Desorption Properties of La-Sr-Co-Fe-O Perovskite-Type Oxide. *J. Therm. Anal. Calorim.* **2014**, *117*, 1221−1229.
(11) Motohashi, T.; Ueda, T.; Masubuchi, Y.; Takiguchi, M.; Setoyama, T.; Oshima, K.; Kikkawa, S. Remarkable Oxygen Intake/Release Capability of $BaYMn_2O_{5+\delta}$: Applications to Oxygen Storage Technologies. *Chem. Mater.* **2010**, *22*, 3192−3196.
(12) Lein, H.; Wiik, K.; Grande, T. Kinetic Demixing and Decomposition of Oxygen Permeable Membranes. *Solid State Ionics* **2006**, *177*, 1587−1590.
(13) Jalili, H.; Chen, Y.; Yildiz, B. Structural, Chemical, and Electronic State on $La_{0.7}Sr_{0.3}MnO_3$ Dense Thin-Film Surfaces at High Temperature: Surface Segregation. *ECS Trans.* **2010**, *28*, 235−240.
(14) Remsen, S.; Dabrowski, B. Synthesis and Oxygen Storage Capacities of Hexagonal Dy 1− x Y x MnO 3+δ. *Chem. Mater.* **2011**, *23*, 3818−3827.
(15) Abughayada, C.; Dabrowski, B.; Kolesnik, S.; Brown, D. E.; Chmaissem, O. Characterization of Oxygen Storage and Structural Properties of Oxygen-Loaded Hexagonal $RMnO_{3+\delta}$ (R = Ho, Er, and Y). *Chem. Mater.* **2015**, *27*, 6259−6267.
(16) Bergum, K.; Okamoto, H.; Fjellvåg, H.; Grande, T.; Einarsrud, M. A.; Selbach, S. M. Synthesis, Structure and Magnetic Properties of Nanocrystalline $YMnO_3$. *Dalton Trans.* **2011**, *40*, 7583−7589.
(17) Evans, D. M.; Holstad, T. S.; Mosberg, A. B.; Småbråten, D. R.; Vullum, P. E.; Dadlani, A. L.; Shapovalov, K.; Yan, Z.; Bourret, E.; Gao, D.; Akola, J.; Torgersen, J.; van Helvoort, A. T. J.; Selbach, S. M.; Meier, D. Conductivity Control via Minimally Invasive Anti-Frenkel Defects in a Functional Oxide. *Nat. Mater.* **2020**, *19*, 1195−1200.
(18) Skjærvø, S. H.; Wefring, E. T.; Nesdal, S. K.; Gaukås, N. H.; Olsen, G. H.; Glaum, J.; Tybell, T.; Selbach, S. M. Interstitial Oxygen as a Source of P-Type Conductivity in Hexagonal Manganites. *Nat. Commun.* **2016**, *7*, No. 13745.
(19) van Roosmalen, J. A. M.; Cordfunke, E. H. P. The Defect Chemistry of $LaMnO_{3\pm\delta}$ − 4. Defect Model for $LaMnO_{3+\delta}$. *J. Solid State Chem.* **1994**, *110*, 109−112.
(20) Griffin, S. M.; Reidulff, M.; Selbach, S. M.; Spaldin, N. A. Defect Chemistry as a Crystal Structure Design Parameter: Intrinsic Point Defects and Ga Substitution in $InMnO_3$. *Chem. Mater.* **2017**, *29*, 2425−2434.
(21) Kotomin, E. A.; Mastrikov, Y. A.; Heifets, E.; Maier, J. Adsorption of Atomic and Molecular Oxygen on the $LaMnO_3$ (001) Surface: Ab Initio Supercell Calculations and Thermodynamics. *Phys. Chem. Chem. Phys.* **2008**, *10*, 4644−4649.
(22) Polfus, J. M.; Yildiz, B.; Tuller, H. L. Origin of Fast Oxide Ion Diffusion along Grain Boundaries in Sr-Doped $LaMnO_3$. *Phys. Chem. Chem. Phys.* **2018**, *20*, 19142−19150.
(23) Carrasco, J.; Illas, F.; Lopez, N.; Kotomin, E. A.; Zhukovskii, Y. F.; Evarestov, R. A.; Mastrikov, Y. A.; Piskunov, S.; Maier, J. First-Principles Calculations of the Atomic and Electronic Structure of F Centers in the Bulk and on the (001) Surface of $SrTiO_3$. *Phys. Rev. B* **2006**, *73*, No. 064106.
(24) Abughayada, C.; Dabrowski, B.; Avdeev, M.; Kolesnik, S.; Remsen, S.; Chmaissem, O. Structural, Magnetic, and Oxygen Storage Properties of Hexagonal $Dy_{1-x}Y_xMnO_{3+\delta}$. *J. Solid State Chem.* **2014**, *217*, 127−135.
(25) Parkkima, O.; Malo, S.; Hervieu, M.; Rautama, E. L.; Karppinen, M. New $RMnO_{3+\delta}$ (R = Y, Ho; Δ≈0.35) Phases with Modulated Structure. *J. Solid State Chem.* **2015**, *221*, 109−115.
(26) Świerczek, K.; Klimkowicz, A.; Nishihara, K.; Kobayashi, S.; Takasaki, A.; Alanizy, M.; Kolesnik, S.; Dabrowski, B.; Seong, S.; Kang, J. Oxygen Storage Properties of Hexagonal $HoMnO_{3+\delta}$. *Phys. Chem. Chem. Phys.* **2017**, *19*, 19243−19251.
(27) Moreno Botello, Z. L.; Montenegro, A.; Grimaldos Osorio, N.; Huvé, M.; Pirovano, C.; Småbråten, D. R.; Selbach, S. M.; Caneiro, A.; Roussel, P.; Gauthier, G. H. Pure and Zr-Doped $YMnO_{3+\delta}$ as a YSZ-Compatible SOFC Cathode: A Combined Computational and Experimental Approach. *J. Mater. Chem. A* **2019**, *7*, 18589−18602.
(28) Klimkowicz, A.; Cichy, K.; Chmaissem, O.; Dabrowski, B.; Poudel, B.; Świerczek, K.; Taddei, K. M.; Takasaki, A. Reversible Oxygen Intercalation in Hexagonal $Y_{0.7}Tb_{0.3}MnO_{3+\delta}$: Toward Oxygen Production by Temperature-Swing Absorption in Air. *J. Mater. Chem. A* **2019**, *7*, 2608−2618.
(29) Cichy, K.; Świerczek, K.; Jarosz, K.; Klimkowicz, A.; Marzec, M.; Gajewska, M.; Dabrowski, B. Towards Efficient Oxygen Separation from Air: Influence of the Mean Rare-Earth Radius on Thermodynamics and Kinetics of Reactivity with Oxygen in Hexagonal $Y_{1-x}R_xMnO_{3+\delta}$. *Acta Mater.* **2021**, *205*, No. 116544.
(30) Klimkowicz, A.; Hashizume, T.; Cichy, K.; Tamura, S.; Świerczek, K.; Takasaki, A.; Motohashi, T.; Dabrowski, B. Oxygen Separation from Air by the Combined Temperature Swing and Pressure Swing Processes Using Oxygen Storage Materials $Y_{1-x}(Tb/Ce)_xMnO_{3+\delta}$. *J. Mater. Sci.* **2020**, *55*, 15653−15666.
(31) Selbach, S. M.; Løvik, A. N.; Bergum, K.; Tolchard, J. R.; Einarsrud, M. A.; Grande, T. Crystal Structure, Chemical Expansion and Phase Stability of $HoMnO_3$ at High Temperature. *J. Solid State Chem.* **2012**, *196*, 528−535.
(32) Bos, J.-W. G.; van Aken, B. B.; Palstra, T. T. M. Site Disorder Induced Hexagonal-Orthorhombic Transition in $Y_{1-x}^{3+}$ $Gd_x^{3+}MnO_3$. *Chem. Mater.* **2001**, *13*, 4804−4807.
(33) Brinks, H. W.; Rodríguez-Carvajal, J.; Fjellvåg, H.; Kjekshus, A.; Hauback, B. C. Crystal and Magnetic Structure of Orthorhombic $HoMnO_3$. *Phys. Rev. B* **2001**, *63*, No. 204.
(34) Asaka, T.; Nemoto, K.; Kimoto, K.; Arima, T.; Matsui, Y. Crystallographic Superstructure of Ti-Doped Hexagonal $YMnO_3$. *Phys. Rev. B* **2005**, *71*, No. 317.
(35) Gibbs, A. S.; Knight, K. S.; Lightfoot, P. High-Temperature Phase Transitions of Hexagonal $YMnO_3$. *Phys. Rev. B* **2011**, *83*, No. 1958.
(36) Huang, Y. H.; Fjellvåg, H.; Karppinen, M.; Hauback, B. C.; Yamauchi, H.; Goodenough, J. B. Crystal and Magnetic Structure of the Orthorhombic Perovskite $YbMnO_3$. *Chem. Mater.* **2006**, *18*, 2130−2134.
(37) Zhou, J.-S.; Goodenough, J. B.; Gallardo-Amores, J. M.; Morán, E.; Alario-Franco, M. A.; Caudillo, R. Hexagonal versus Perovskite Phase of Manganite $RMnO_3$ (R = Y, Ho, Er, Tm, Yb, Lu). *Phys. Rev. B* **2006**, *74*, No. 725.
(38) Brinks, H. W.; Fjellvåg, H.; Kjekshus, A. Synthesis of Metastable Perovskite-Type $YMnO_3$ and $HoMnO_3$. *J. Solid State Chem.* **1997**, *129*, 334−340.
(39) Cichy, K.; Świerczek, K. Influence of Doping on the Transport Properties of $Y_{1-x}Ln_xMnO_{3+\delta}$ (Ln: Pr, Nd). *Crystals* **2021**, *11*, No. 510.
(40) Cichy, K.; Zając, M.; Świerczek, K. Evaluation of Applicability of Nd- and Sm-Substituted $Y_{1-x}R_xMnO_{3+\delta}$ in Temperature Swing Absorption for Energy-Related Technologies. *Energy* **2022**, *239*, No. 122429.
(41) Otomo, M.; Hasegawa, T.; Asakura, Y.; Yin, S. Remarkable Effects of Lanthanide Substitution for the Y-Site on the Oxygen


https://doi.org/10.1021/acs.chemmater.3c00189
Chem. Mater. 2023, 35, 5764−5776

Storage/Release Performance of $YMnO_{3+\delta}$. *ACS Appl. Mater. Interfaces* **2021**, *13*, 31691−31698.
(42) Aikawa, Y.; Katsufuji, T.; Arima, T.; Kato, K. Effect of Mn Trimerization on the Magnetic and Dielectric Properties of Hexagonal $YMnO_3$. *Phys. Rev. B* **2005**, *71*, No. 184418.
(43) Levin, I.; Krayzman, V.; Vanderah, T. A.; Tomczyk, M.; Wu, H.; Tucker, M. G.; Playford, H. Y.; Woicik, J. C.; Dennis, C. L.; Vilarinho, P. M. Oxygen-Storage Behavior and Local Structure in Ti-Substituted $YMnO_3$. *J. Solid State Chem.* **2017**, *246*, 29−41.
(44) Lilienblum, M.; Lottermoser, T.; Manz, S.; Selbach, S. M.; Cano, A.; Fiebig, M. Ferroelectricity in the Multiferroic Hexagonal Manganites. *Nat. Phys.* **2015**, *11*, 1070−1073.
(45) Fennie, C. J.; Rabe, K. M. Ferroelectric Transition in $YMnO_3$ from First Principles. *Phys. Rev. B* **2005**, *72*, No. 100103(R).
(46) Skjærvø, S. H.; Meier, Q. N.; Feygenson, M.; Spaldin, N. A.; Billinge, S. J. L.; Bozin, E. S.; Selbach, S. M. Unconventional Continuous Structural Disorder at the Order-Disorder Phase Transition in the Hexagonal Manganites. *Phys. Rev. X* **2019**, *9*, No. 31001.
(47) Asakura, Y.; Miyake, A.; Otomo, M.; Yin, S. Improvement of the $O_2$ Storage/Release Rate of $YMnO_3$ Nanoparticles Synthesized by the Polymerized Complex Method. *Dalton Trans.* **2020**, *49*, 966−971.
(48) Han, L.; Zhou, Z.; Bollas, G. M. Heterogeneous Modeling of Chemical-Looping Combustion. Part 2: Particle Model. *Chem. Eng. Sci.* **2014**, *113*, 116−128.
(49) Cao, S.; Tao, F. F.; Tang, Y.; Li, Y.; Yu, J. Size- and Shape-Dependent Catalytic Performances of Oxidation and Reduction Reactions on Nanocatalysts. *Chem. Soc. Rev.* **2016**, *45*, 4747−4765.
(50) Grande, T.; Tolchard, J. R.; Selbach, S. M. Anisotropic Thermal and Chemical Expansion in Sr-Substituted LaMnO3+$\delta$: Implications for Chemical Strain Relaxation. *Chem. Mater.* **2012**, *24*, 338−345.
(51) Klimkowicz, A.; Świerczek, K.; Kobayashi, S.; Takasaki, A.; Allahyani, W.; Dabrowski, B. Improvement of Oxygen Storage Properties of Hexagonal YMnO3+$\delta$ by Microstructural Modifications. *J. Solid State Chem.* **2018**, *258*, 471−476.
(52) Coelho, A. A. TOPAS and TOPAS-Academic: An Optimization Program Integrating Computer Algebra and Crystallographic Objects Written in C++. *J. Appl. Crystallogr.* **2018**, *51*, 210−218.
(53) Evans, J. S. O. Advanced Input Files & Parametric Quantitative Analysis Using Topas. *Mater. Sci. Forum* **2010**, *651*, 1−9.
(54) Kluyver, T.; Ragan-Kelley, B.; Pérez, F.; Granger, B.; Bussonnier, M.; Frederic, J.; Kelley, K.; Hamrick, J.; Grout, J.; Corlay, S.; Ivanov, P.; Avila, D.; Abdalla, S.; Willing, C.*Jupyter Notebooks—a Publishing Format for Reproducible Computational Workflows*, Positioning and Power in Academic, Players, Agents and Agendas, Proceedings of the 20th International Conference on Electronic Publishing, 2016; pp 87−90.
(55) Kresse, G.; Hafner, J. Ab Initio Molecular Dynamics for Liquid Metals. *Phys. Rev. B* **1993**, *47*, 558−561.
(56) Kresse, G.; Hafner, J. Ab Initio Molecular-Dynamics Simulation of the Liquid-Metalamorphous- Semiconductor Transition in Germanium. *Phys. Rev. B* **1994**, *49*, 14251−14269.
(57) Kresse, G.; Furthmüller, J. Efficient Iterative Schemes for Ab Initio Total-Energy Calculations Using a Plane-Wave Basis Set. *Phys. Rev. B* **1996**, *54*, 11169−11186.
(58) Kresse, G.; Furthmüller, J. Efficiency of Ab-Initio Total Energy Calculations for Metals and Semiconductors Using a Plane-Wave Basis Set. *Comput. Mater. Sci.* **1996**, *6*, 15−50.
(59) Perdew, J. P.; Burke, K.; Ernzerhof, M. Generalized Gradient Approximation Made Simple. *Phys. Rev. Lett.* **1996**, *77*, 3865−3868.
(60) Blöchl, P. E. Projector Augmented-Wave Method. *Phys. Rev. B* **1994**, *50*, 17953−17979.
(61) Dudarev, S. L.; Botton, G.; et al. Electron-Energy-Loss Spectra and the Structural Stability of Nickel Oxide: An LSDA+U Study. *Phys. Rev. B* **1998**, *57*, 1505−1509.
(62) Wang, L.; Maxisch, T.; Ceder, G. Oxidation Energies of Transition Metal Oxides within the GGA+*U* Framework. *Phys. Rev. B* **2006**, *73*, No. 195107.
(63) Tripathi, S.; Petkov, V.; Selbach, S. M.; Bergum, K.; Einarsrud, M. A.; Grande, T.; Ren, Y. Structural Coherence and Ferroelectric Order in Nanosized Multiferroic $YMnO_3$. *Phys. Rev. B* **2012**, *86*, No. 094101.
(64) Shannon, R. D. Revised Effective Ionic Radii and Systematic Studies of Interatomic Distances in Halides and Chalcogenides. *Acta Crystallogr., Sect. A* **1976**, *32*, 751−767.
(65) Van Aken, B. B.; Bos, J.; de Groot, R. A.; Palstra, T. T. Asymmetry of Electron and Hole Doping in $YMnO_3$. *Phys. Rev. B* **2001**, *63*, No. 125127.
(66) Holstad, T. S.; Evans, D. M.; Ruff, A.; Småbråten, D. R.; Schaab, J.; Tzschaschel, C.; Yan, Z.; Bourret, E.; Selbach, S. M.; Krohns, S.; Meier, D. Electronic Bulk and Domain Wall Properties in B -Site Doped Hexagonal $ErMnO_3$. *Phys. Rev. B* **2018**, *97*, No. 085143.
(67) Marthinsen, A.; Grande, T.; Selbach, S. M. Microscopic Link between Electron Localization and Chemical Expansion in $AMnO_3$ and $ATiO_3$ Perovskites (A = Ca, Sr, Ba). *J. Phys. Chem. C* **2020**, *124*, 12922−12932.
(68) Remsen, S.; Dabrowski, B.; Chmaissem, O.; Mais, J.; Szewczyk, A. Synthesis and Oxygen Content Dependent Properties of Hexagonal $DyMnO_{3+\delta}$. *J. Solid State Chem.* **2011**, *184*, 2306−2314.
(69) Bakken, E.; Norby, T.; Stølen, S. Redox Energetics of Perovskite-Related Oxides. *J. Mater. Chem.* **2002**, *12*, 317−323.
(70) Vieten, J.; Bulfin, B.; Senholdt, M.; Roeb, M.; Sattler, C.; Schmücker, M. Redox Thermodynamics and Phase Composition in the System $SrFeO_{3-\delta}$ — $SrMnO_{3-\delta}$. *Solid State Ionics* **2017**, *308*, 149−155.
(71) Rørmark, L.; Mørch, A. B.; Wiik, K.; Stølen, S.; Grande, T. Enthalpies of Oxidation of $CaMnO_{3-\delta}$, $Ca_2MnO_{4-\delta}$ and $SrMnO_{3-\delta}$ Deduced Redox Properties. *Chem. Mater.* **2001**, *13*, 4005−4013.
(72) Han, D.; Uda, T.; Nose, Y.; Okajima, T.; Murata, H.; Tanaka, I.; Shinoda, K. Tetravalent Dysprosium in a Perovskite-Type Oxide. *Adv. Mater.* **2012**, *24*, 2051−2053.
(73) Bakken, E.; Norby, T.; Stølen, S. Nonstoichiometry and Reductive Decomposition of $CaMnO_{3-\delta}$. *Solid State Ionics* **2005**, *176*, 217−223.
(74) Bakken, E.; Boerio-Goates, J.; Grande, T.; Hovde, B.; Norby, T.; Rørmark, L.; Stevens, R.; Stølen, S. Entropy of Oxidation and Redox Energetics of $CaMnO_{3-\delta}$. *Solid State Ionics* **2005**, *176*, 2261−2267.
(75) Mohn, C. E.; Allan, N. L.; Freeman, C. L.; Ravindran, P.; Stølen, S. Collective Ionic Motion in Oxide Fast-Ion-Conductors. *Phys. Chem. Chem. Phys.* **2004**, *6*, 3052−3055.


https://doi.org/10.1021/acs.chemmater.3c00189
*Chem. Mater.* 2023, 35, 5764−5776